DOI: 10.13009/EUCASS2023-638
Aerospace Europe Conference 2023 – 10TH EUCASS – 9TH CEAS

Cold-Gas Experiments on Advanced Nozzles in Subsonic Counter-Flows

Giuseppe Scarlatella [a†], Theodor Heutling [a], Jan Sieder-Katzmann [a], Felix Weber [b], Marco Portolani [c], Marco Garutti [d], Daniele Bianchi [b], Andrea Ferrero [c], Dario G. Pastrone [c], Martin Tajmar [a] and Christian Bach [a]

[a] *Technische Univeristät Dresden, Chair of Space Systems*
Marschnerstraße 32, 01307 Dresden, Germany
giuseppe.scarlatella@tu-dresden.de · theodor.heutling@tu-dresden.de · jan.sieder-katzmann@tu-dresden.de
martin.tajmar@tu-dresden.de · christian.bach1@tu-dresden.de
[b] *Università di Roma "La Sapienza", Department of Mechanical and Aerospace Engineering (DIMA)*
Via Eudossiana 18, 00183 Rome, Italy
felix.weber@uniroma1.it · daniele.bianchi@uniroma1.it
[c] *Politecnico di Torino, Department of Mechanical and Aerospace Engineering (DIMEAS)*
Corso Duca degli Abruzzi 24, 10129 Torino, Italy
marco.portolani@studenti.polito.it · andrea_ferrero@polito.it · dario.pastrone@polito.it
[d] *Università degli Studi di Padova, Department of Industrial Engineering (DII)*
Via 8 Febbraio 2, 35122 Padova, Italy
marco.garutti@studenti.unipd.it
[†]Corresponding author

Abstract

The experimental campaign at Technische Universität Dresden tests the performance of annular-aerospike, dual-bell and expansion-deflection nozzles compared with conventional nozzles in various subsonic counter-flow regimes and atmospheric conditions. This manuscript offers comparative results between advanced nozzles (aerospike and expansion-deflection) and conventional nozzles, insights on the methods of analysis, the processing of the experimental data and the interconnections with the numerical simulations on advanced nozzles in retro-flow configuration by the institute. As final outcome, the experimental campaign delivers early results on the feasibility of adopting advanced nozzles as solution for the main propulsion system of the upcoming class of reusable launch vehicles.

List of Abbreviations/Acronyms

AI	Aerodynamics Interference
ALM	Additive Layer Manufacturing
AN	Aerospike Nozzle
ANC	Advanced Nozzle Concepts
AOA	Angle-Of-Attack
AR	Aspect Ratio
BOS	Background-Oriented Schlieren
CFD	Computational Fluid Dynamics
DAQ	Data Acquisition (system)
DB	Dual-Bell (nozzle)
DOF	Degree-Of-Freedom
ED	Expansion-Deflection (nozzle)
NPR	Nozzle Pressure Ratio
RLV	Reusable Launch Vehicle
SLS	Sea-Level-Standard
TRL	Technology Readiness Level
TUD	Technische Universität Dresden
TVC	Thrust Vectoring Control
VTVL	Vertical Take-Off Vertical Landing

DOI: 10.13009/EUCASS2023-638

1. Introduction

In recent years, there has been growing interest in Advanced Nozzle Concepts[1] (ANCs), such as Aerospike Nozzles (ANs), Dual-Bell (DB) and Expansion-Deflection (ED) nozzles, and their application to Reusable Launch Vehicles (RLVs). This is ascribable to their intrinsic altitude compensation properties, which could mitigate the additional propellant cost resulting from the vertical landing manoeuvres based on retro-propulsion[2]. Additionally, design solutions recently investigated, such as film-cooling transition control for DB nozzles[3] and Additive Layer Manufacturing (ALM) techniques for regenerative cooling of aerospike engines[4], could overcome the current technical limitations of these architectures. Despite of a relatively low technology readiness level w.r.t. conventional bell nozzles, further investigations on ANCs in retro-flow scenarios could improve the understanding of the physics of retro-propulsion. Eventually, the adaptation of ANCs to the upcoming class of reusable launchers could advance the technology for full recovery of the main stage, thus increasing competitiveness of Europe by lowering down costs of access to space.

This manuscript offers an overview on the experimental activities at Technische Universität Dresden (TUD) that involve advanced nozzles in retro-propulsive scenarios. More specifically, small-scaled additively manufactured nozzles are tested with cold-flows and invested by various subsonic free-stream regimes[5]. These scenarios, namely *counter-flows* (free-stream only) and *retro-flows* (nozzle-jet and free-stream interaction), are described in terms of both aerodynamic performance and nozzle performance. In order to do so, a brief recap about the methods of investigation (extended by references to previous publications[5]) is offered to the reader in Section 2, together with an overview of the test-facility, a detailed description of the latest updates to the setup and the adopted nozzle-models in Section 3. Subsequently, in Section 4 it is presented a preliminary test-campaign to characterise the subsonic free-stream, followed by an overview of the experimental activities and results for nozzle performance and aerodynamic performance of the extended body in Section 5 and Section 6, respectively. A discussion on the results, together with a comparison with parallel CFD studies is given in Section 7. Eventually, the limits of the given methodology and envisaged improvements are identified, concluding with an outlook on future research activities in Section 8.

2. Methods

The proposed methodology aims to simulate conditions in analogy to landing-burn manoeuvres for Vertical Take-Off and Landing (VTVL) RLVs such as SpaceX's Falcon 9[2,6–8], during which the reusable main-stage decelerates through the denser layers of the atmosphere through a powered-descent, namely retro-propulsion. During this manoeuvre, both descent-velocity and ambient-pressure along the trajectory vary drastically (starting from altitudes of $5-10\,\mathrm{km}$ to sea-level, from low-supersonic to low-subsonic/motionless[2]). The Vacuum Wind Tunnel facility in TUD (see Fig. 1) offers free-stream velocities up to a maximum of $\sim 100\,\mathrm{m/s}$ and a minimum of $\sim 7\,\mathrm{kPa}$ for ambient-pressure. This is sufficient to study in Mach and Reynolds analogy[9,10] (refer Section 6) a wide portion of external conditions experienced during a typical landing-burn manoeuvre.

The analysis of phenomena treats both nozzle performance and aerodynamic performance: the first are described in terms of *thrust* (T), *specific-impulse* (I_{sp}) and *nozzle-thrust-coefficient* (or simply *thrust-coefficient*, C_F)[11] by following a method of analysis in agreement with their definitions[5,11]; the analysis of aerodynamic performance distinguishes between nozzle contribution and aerodynamic contribution to the overall drag (D) and drag-coefficient (C_D)[10,12]. More specifically:

$$C_D = \frac{D}{q_\infty A_{ref}} = \frac{\tau + D_{aero}}{q_\infty A_{ref}} \tag{1}$$

where τ is the effective thrust resulting from the interaction between nozzle-jet and free-stream, D_{aero} is the contribution of the aerodynamics to the drag (i.e., viscous-drag, induced-drag, wave-drag), q_∞ is the *dynamic-pressure* of the free-stream and A_{ref} is a reference-area, commonly the *cross-sectional area* of the vehicle (A_B). The Eq. 1 can be split in its main contributions:

$$C_T = \frac{\tau}{q_\infty A_B} \tag{2}$$

$$C_{D_{aero}} = \frac{D_{aero}}{q_\infty A_B} \tag{3}$$

DOI: 10.13009/EUCASS2023-638

The Eq. 2 and 3 define the *aerodynamics-thrust-coefficient*[10] (C_T, not to be confused with C_F) and the *aerodynamics-drag-coefficient* ($C_{D_{aero}}$), respectively. These values describe the contribution of propulsion and aerodynamics to the overall drag for various regimes of dynamic-pressure during a retro-propulsion manoeuvre. An analogous approach for the lift is plausible but it is not treated in this manuscript, as only cases for a null Angle-Of-Attack (AOA) and absence of Thrust-Vectoring-Control (TVC) are reported.

For as intuitive such methodology might appear, indeed it hides the complex interconnections between the effective nozzle performance and the aerodynamics of the vehicle in terms of τ and $C_{D_{aero}}$, which depend on a multitude of factors and still constitute the greatest unknowns in the physics of retro-propulsion. Formerly, thrust-induced drag and aerodynamic-drag should not be separated. Nevertheless, in the specific case of subsonic free-streams in incompressible-flow regimes ($M_\infty < 0.3$), the influence of the counter-flow on the nozzle performance is expected to be relatively small, thus it is temporarily assumed that the effects of the interaction are negligible ($\tau \approx T$). This comes as a first step of investigation, in order to provide valuable estimates of the performance before adopting a more realistic approach for future research activities. Nevertheless, this assumption will be re-discussed in Section 7, by quantifying the actual impact of the subsonic free-stream through comparison with numerical results.

For comparing the aerodynamic performance between counter-flows and retro-flows (for identical free-stream conditions), it is useful to study the increment/decrement (in percentage) of drag-coefficients. So, here are defined:

$$\Delta C_D = \frac{C_{D_{RFL}} - C_{D_{CFL}}}{C_{D_{CFL}}} \times 100\,\% \tag{4}$$

$$\Delta C_{D_{aero}} = \frac{(C_{D_{aero}})_{RFL} - C_{D_{CFL}}}{C_{D_{CFL}}} \times 100\,\% \tag{5}$$

Generally, one expects the overall C_D to increase in retro-propulsive phases as it now includes the contribution of the thrust. Indeed, the vehicle tends to slow-down faster for high *thrust-to-weight* ratios, as a strong decrement of the *ballistic-coefficient* occurs ($\beta = M/(C_D A_B)$, with M as the total mass of the vehicle and a generally higher C_D due to retro-propulsion). On the other hand, the aerodynamic contribution to C_D is expected to diminish drastically, as the nozzle-jet essentially behaves as a blunt-body in the Aerodynamics Interference (AI) area. In re-entry manoeuvres for reusable-rockets, the latter is generated by the interaction between rocket-engine exhaust-plumes and the asymptotic free-stream[10], which is replicated by the experiments as the interaction between nozzle-jet and counter-flow (refer Section 6). The AI region establishes in front of the baseplate, and it scales with C_T (a clear correlation is verified for supersonic free-streams[10] if $C_T > 1.0$ and nozzle-jet is under-expanded, with a strong discontinuity in the range $1.0 < C_T < 2.0$ when switching from *jet-penetration-mode* to *blunt-mode*).

3. Setup & Test-bench

This section focuses mostly on the latest iteration of the setup (refer Section 3.2) and the nozzle-models involved in the experimental activities (refer Section 3.3). A more detailed description of the test-facility as well as a detailed list of types/technical-characteristics of the sensors mounted on the test-bench is provided in a previous publication[5]. Nevertheless, some recalls are included in Section 3.1 in order to facilitate the reading.

3.1 Test facility

In Fig. 1 a schematics of the Vacuum Wind Tunnel at TUD is provided. Its main sub-components of interest for the experimental activities here reported are the test-chamber (or experimental-room), the evacuation-units activated for the performance tests at near-vacuum conditions (see Section 5), the fan/driving-motor for the generation of the conical free-stream and the pre-chamber (here total-pressure is measured to provide a reference velocity for the counter-flow, more details in Section 4). Additionally, the test-chamber hosts a Background-Oriented Schlieren[13] (BOS) optical system for the flow-visualisation. The evacuation units are a Bush RU 0025E and a Bacon V95-GRD-35, which allow the generation of near-vacuum conditions (~ 7 kPa), while the asynchronous driving-motor is an ABB M2QA-II 180 speed-controlled in 0.1 Hz steps from 0-50 Hz (coupled to a radial fan with a diameter of 650 mm, it provides free-stream velocities up to ~ 100 m/s)[14].

DOI: 10.13009/EUCASS2023-638

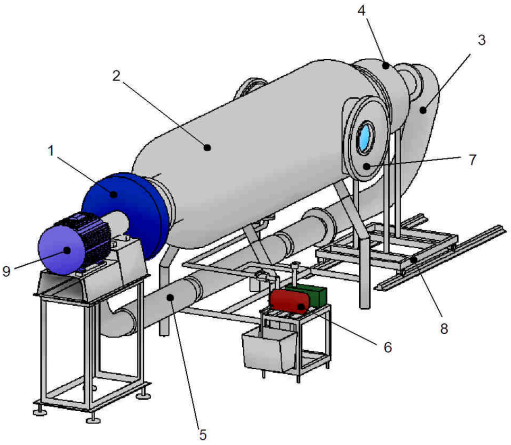

(a) Schematics of the Vacuum-Wind-Tunnel[14].

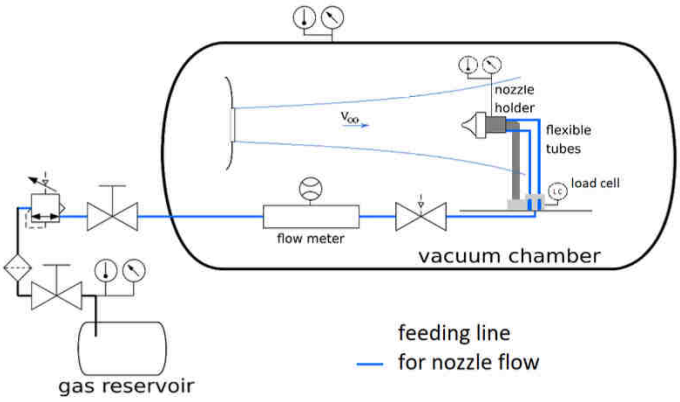

(b) Schematics of test-bench and feed-system.

Figure 1: Details in Figure 1a: (1) fan, (2) experimental room, (3) ring line, (4) pre-chamber (calming boiler), (5) cooling chambers, (6) evacuation units, (7) doors with observation window, (8) shifting device of the pre-chamber, (9) drive motor for free-stream generation. Modified picture, courtesy of M. Leonhardsberger et al.[14].

3.2 Current Setup (latest adaptations)

The concept of the setup is the combination of a pressure chamber hosting interchangeable nozzle-models (additively manufactured with polymeric resins) and a 1-DOF sliding system that allows force measurements through an S-shaped load-cell mounted at the bottom. The previous version of the setup[5] has been modified to reduce the impact of the support structure on the aerodynamic performance evaluation and, more in general, to adapt better to retro-flow tests. More specifically, now it includes an aluminium *body-extension* that brings the original configuration to an Aspect-Ratio ($AR = L_B/D_B$, where L_B is the body-length and D_B is the diameter of the cross-sectional area) closer to a real-case of interest such as Falcon 9. Additionally, it mounts 3D-printed interfaces and frames, together with an add-on to the support-structure to reduce vibrations and bending during retro-flow experiments (see Figures 2).

(a) Picture of the final setup.

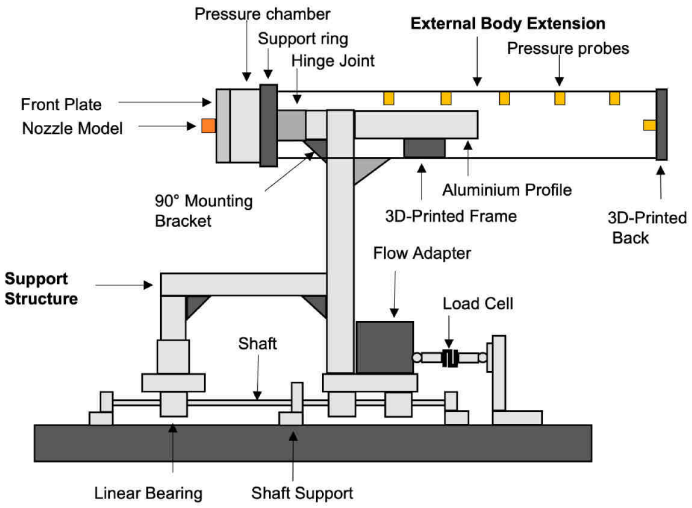

(b) Schematics of the final setup.

Figure 2: Final setup after the latest adaption for testing in retro-flow. Details in Figure 2a: (1) pressure-chamber and nozzle-model, (2) chamber/body interface or support-ring, (3) external body-extension, (4) S-shaped load-cell.

It is due to mention that to realise an $AR = 11.6$ (as Falcon 9 Block 5) would have been not-practical for the installation inside the test-chamber, as well as for the stability of the setup against vibrations induced by the high-density free-streams. Thus, any direct scalability of results to a heavy-lift launcher case-study is limited, as a compromise to advantage the feasibility of the experiments. Nevertheless, the body-extension is long enough to anchor

DOI: 10.13009/EUCASS2023-638

the reattachment-point of the asymptotic stream-current along the side-walls (previous CFD studies[15] confirmed that before the finalisation of the design) and to host a distribution of pressure-probes with sufficient resolution to identify its position through direct measurement of the pressure-coefficient along the wall.

3.3 Nozzle Models

The specimens selected for this manuscript are divided in two categories: continuous altitude-compensating nozzles (i.e., annular aerospike and expansion-deflection concepts) and Rao-parabolic nozzles. The conventional nozzles serve as reference models for the advanced nozzles in terms of performance in both near-vacuum (*RAO-bell_VAC*, see Fig. 3c) and SLS (*RAO-bell_8KM*, see Fig. 3d). The ANCs are designed to provide a thrust level at near-vacuum conditions that is comparable (or identical, at best) to the one of the *RAO-bell_VAC* on design. This was originally planned to be achieved by sharing identical Nozzle-Pressure-Ratio (*NPR*, see Table 1) at on-design conditions and same *expansion-ratio* ($\varepsilon = A_e/A_t = 4.82$, with $= A_e$ as geometrical nozzle-exit-area) but, differently from the conventional nozzle, their altitude-compensation properties allow the ANCs to adapt also to SLS conditions. In this case, their performance are compared to the *RAO-bell_8KM* instead (same *NPR* on design, smaller $\varepsilon = 13.852$), as analytical results predict the *RAO-bell_VAC* to experience high over-expansion and flow-separation[11] in SLS. Additionally, the comparability would be supported even more by the nozzles sharing the same *throat-area* (A_t), thus also sharing the same *mass-flow* ($\dot{m}$) in ideal-case, as direct consequence of identical chamber-pressure and gas-properties. Eventually, the iterative design process on AN and ED nozzle slightly deviated from this approach, as their expansion-ratios converged to $\varepsilon = 4.778$ and $\varepsilon = 6.427$, respectively. For the AN, the ε is practically identical to the one of the RAO-bell for vacuum (0.7 % difference), as the A_t is c.a 4 % smaller in order to achieve the desired thrust or, alternatively, to realise the same exit-mach-number and total mass-flow (as iterative result of the design-tool). On contrary, the ED nozzle needs to adopt a larger ε so to take into account the smaller effective-exit area due to the presence of the pintle. Instead, the other design-parameters left in Table 1 are the same between all the specimens.

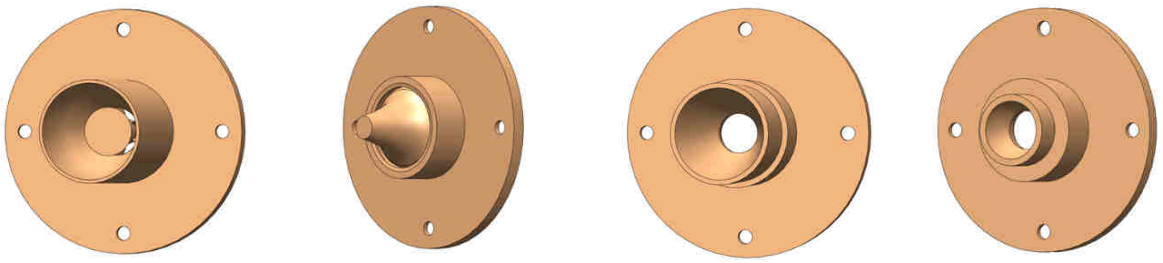

(a) Exp.-Defl. (*ED*) nozzle ($\varepsilon = 6.427$, $NPR = 45.0$).

(b) Aerospike nozzle (*AN*) ($\varepsilon = 4.788$, $NPR = 45.0$).

(c) *RAO-bell_VAC* nozzle ($\varepsilon = 4.82$, $NPR = 45.0$).

(d) *RAO-bell_8KM* nozzle ($\varepsilon = 2.328$, $NPR = 13.852$).

Figure 3: CAD models of *advanced* (a)(b) and *conventional* (c)(d) nozzles. In (a)(b)(c)(d) is specified the geometrical *expansion-ratio* (ε) and *NPR* at their respective design-point.

More details are here provided for the different design approaches identified for each specimen. For the AN the C. C. Lee ideal-contour design-method[16] is adopted, with a truncation length to 45 % of the ideal profile and sonic-conditions at the exit (external supersonic-expansion). The performance losses due to truncation should result below 5 %, but next iterations on this design might increase the efficiency by including a 1-2 % of $\dot{m}$ for the base-bleed[17]. The ED nozzle is designed by Sapienza University by adopting a modified version of the original Angelino's design-method[17] for ideal-contouring of ED nozzles. These nozzles are known for their high aspiration-drag at sea-level for high expansion-ratios[18]. Nevertheless, the ED nozzle was originally included in the comparative also to investigate its effective altitude-compensation against free-streams. The conventional nozzles adopt a classic Rao-parabolic-contour, in agreement with the design parameters suggested in literature[11]. They both share a 80 % length w.r.t. their equivalent conical nozzles (in terms of ε, throat-geometry and chamber-conditions for each), but differ for their design point: the *RAO-bell_VAC* is adapted for near-vacuum operations, its purpose is to verify the performance on-design of the ANCs (same design-point) through a relatively simple design; the *RAO-bell_8KM* presents a lower *NPR* on-design (c.a 30 % of ANCs'), as it is optimised at the same altitude-point in standard conditions of a Merlin 4D engine). This approach allows to quantify the performance-gains of ANCs adapted for vacuum if operating in Sea-Level-Standard (SLS) conditions, also in combination with subsonic free-streams. To better clarify the similarities between the nozzle specimens, an overview of the design-parameters chosen for the nozzles adapted to vacuum operations (i.e., all ANC-models & *RAO-bell_VAC* nozzle) is offered in Table 1.

DOI: 10.13009/EUCASS2023-638

Table 1: Reference design-parameters for nozzle-specimens for vacuum operations[5].

Parameter	**Symbol**	**Value**	**Unit**
Nozzle pressure ratio (on design)	$NPR_{o.d.}$	45.0	-
Chamber total pressure[a]	$p_{c,0}$	0.48	MPa
Chamber total temperature	T_0	293.15	K
Chamber cross-sectional area	A_c	5541.8	mm^2
Isoentropic exponent	γ	1.4	-
Specific gas-constant (air)	R	287	J/kg K
Nozzle throat-area	A_t	58.5	mm^2
Mass-flow[b]	$\dot{m}$	67.3	g/s
Thrust[b]	T	41.6	N

[a]Assumed NPR $\approx p_c/p_{amb}$, as $p_c \approx p_{c,0}$ (for $A_c/A_t \geq 4$)[11].
[b]Ideal values, derived analytically for isoentropic nozzle-flow[11].

Originally, also a DB nozzle (optimised at $NPR = 45.0$) was meant to be part of this comparative study. Unfortunately, the load-cell sensor lost its accuracy due to deterioration/usage during the performance-tests of the DB nozzle, which shall be included in future publications.

4. Counter-flow Characterisation Campaigns

This preliminary test-campaign is carried out without the setup inside the test-chamber, in order to generate counter-flow regimes with a high-level of confidence on the local values of air-speed (together with a verification of the operating conditions of the wind-tunnel after few years of it being not-operational). Indeed, as the conical-flow generated by the wind-tunnel is not uniform (nor laminar) within the full-extension of the test-chamber, it is necessary to locally measure the air-speed in order to determine $M_{x,y}$ and $Re_{x,y}$. These are evaluated by measuring the stagnation conditions and the distribution of local flow-velocity, by assuming the counter-flow-nozzle diameter as reference length for evaluating Re. It should be noted that to measure $u_{x,y}$ during the experiments (e.g., by using Pitót tubes) would influence the flow-field with the presence of other bodies, instead of having a clear area for the Aerodynamics Interference (AI). Additionally, this disturbances would compromise the distribution of air-speed in the laminar-core of the counter-flow, as well as the aerodynamic performance on the body-extension.

For these reasons, this test-campaign aimed to characterise the counter-flows by mapping a velocity-distribution in the test-chamber, for various u_0 regimes. The free-stream is assumed as an axial-symmetric conical-flow (see Figure 4), characterised by a laminar-core (AI-area), a mixing-region towards turbulent regimes and a fully-developed turbulent area (pressure-chamber and body-extension areas).

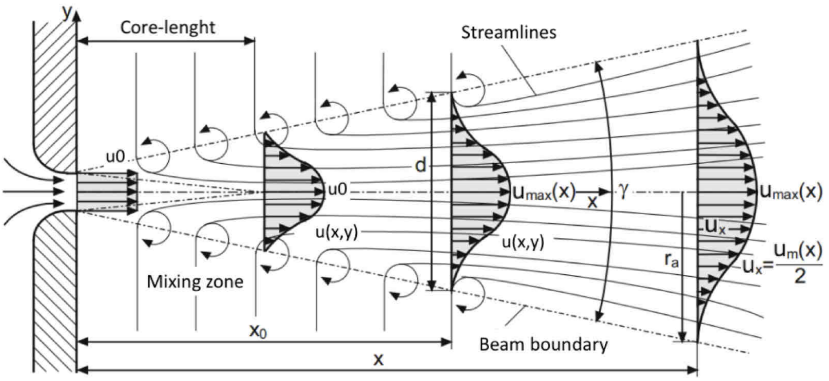

Figure 4: Geometric parameters of the conical free-jet (counter-flow). Modified picture, courtesy of M. Leonhardsberger et al.[14].

The geometrical parameters in Figure 4 are: u_0 (maximum air-speed at free-jet-nozzle-exit), u_x (axial-velocity component of the free-jet at axis-of-symmetry), $u_{x,y}$ (general axial-velocity component in hypotesis of axial-symmetric

DOI: 10.13009/EUCASS2023-638

development of conical-flow). For incompressible flows ($M_\infty < 0.3$) the Bernoulli's equation is valid, thus the maximum counter-flow speed at nozzle exit (u_0) is calculated from the difference between absolute stagnation pressures in the pre-chamber ($p_{pre-ch.,0}$) and test-chamber ($p_{test-ch.,0} \equiv p_{amb}$) (see Figure 1). Intuitively, in presence of a free-stream the first is higher than the ambient-pressure (as the mechanical action of the fan increases the total enthalpy of the flow). In absence of losses, the u_0 (at the free-jet-nozzle-exit) would measures exactly:

$$u_0 = \sqrt{\frac{2(p_{pre-ch.} - p_{amb})}{\rho_{amb}}} \tag{6}$$

where ρ is evaluated before starting the tests and comes from ideal-gas law (preliminary evaluation of p_{amb} and T_{amb}). Differently from Figure 4, the $u_{x=0} = (u_x)_{MAX}$ rarely equals the u_0 at the free-jet nozzle-exit, because of additional losses during the subsonic-expansion in the pre-chamber, so u_0 loses its physical connotation and assumes meaning of an *ideal maximum air-speed value*, dependent only on the fan frequency and the ambient conditions, here adopted to describe the flow-field in dimensionless air-speed terms.

This methodology allows to derive the linear relationship $f - u_0$, where f is the fan-frequency, constructed by interpolating four detections at different frequencies ($f = 22.9, 30.4, 35.7, 39.5\,Hz$) in close-to-SLS conditions. This relationship is dependant on ambient conditions, thus it is corrected by a factor $\sqrt{\rho_{SLS}/\rho_{exp}}$ to obtain more accurate results (with ρ_{exp} being the value of density at the time of the test), in agreement with Eq. 6.

The following step is to derive a normalised air-speed map, that can deliver values of $u_{x,y}$ for different u_0 (see Figure 5a). The dimensionless air-speed values remain constant over the velocity ranges of interest[14], thus the flow-characterization data remain valid for various u_0. Up to 20 measurement points were selected ($x/D = 0.0, 2.0, 4.0, 6.0$ and $y/R = 0.0, 0.5, 1.0, 1.5, 2.0$, excluding points (0.0,1.5) and (0.0,2.0) due to zero average-velocity. An additional measurement at (2.0,0.75) was added to better characterize the curve at $x/D = 2.0$. The measurements were taken twice for each point and averaged over a 10-second interval. The final result is the average air-speed of the values in Figure 5a. In closure, a Matlab script was used to interpolate the data using cubic splines and the measured data were mirrored for negative values of y/R in hypothesis of axial-symmetric conical-flow.

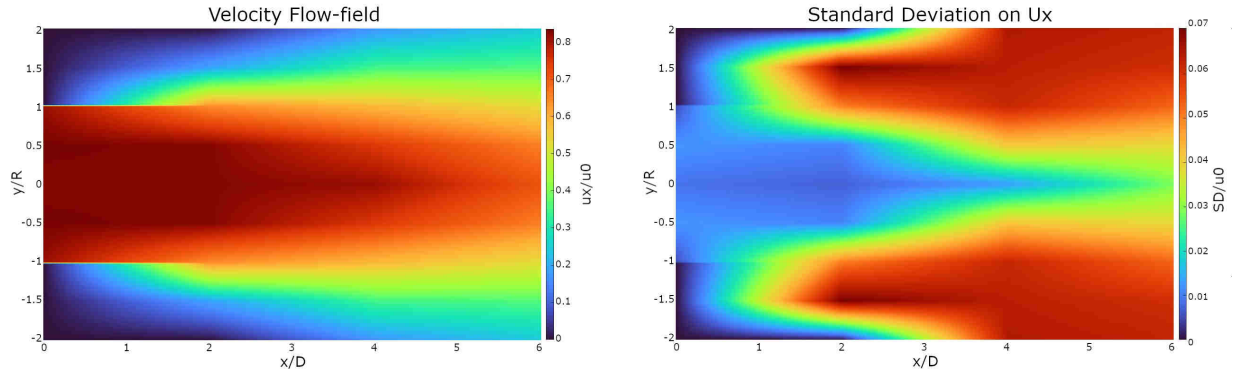

(a) Experimental-map of *averaged-values* (u_x/u_0).

(b) Experimental-map of *standard-deviation* (u_x/u_0).

Figure 5: Counter-flow characterisation (velocity flow-field) in hypothesis of axial-symmetric distribution[19].

The 2D-map in Figure 5a allows to predict the $u_{x,y}$ for different values of u_0, while the Standard-Deviation map in Figure 5b gives a qualitative indication of the extension of the laminar-core. This reaches up to $x/D = 5 \div 6$, thus providing an indication about the maximum distance where to place the setup (*baseplate-distance-from-freestream-nozzle*, namely d). The laminar-core hypothesis (sufficiently verified for $(u_x)_{SD}/u_0 < 0.3$ in Figure 5b) ensures a compatibility of AI fluid dynamics between experiments and CFD simulated in uniform free-streams. The same cannot be said for the aerodynamic performance on the body, which on contrary is invested by a free-jet that is transitioning to a fully-developed turbulent regime. This limitation is discussed in further details in Section 8.

DOI: 10.13009/EUCASS2023-638

5. Performance Campaign

The performance evaluation of the nozzle-specimens is carried out in order to verify their design and effective altitude-compensation in absence of counter-flows (refer Section 5.2). Moreover, in hypothesis of $\tau \approx T$ (refer Section 2), the performance can also be used to estimate C_T and $C_{D_{aero}}$ during retro-flow experiments. Such assumption is necessary in absence of a dedicated sensor for an isolated measurement of T during retro-flows operations and its limitations are further discussed in Section 8. In order to achieve reliable nozzle performance at on-design and SLS conditions, a multiple-step approach and corrections to the experimental values are needed (refer Section 5.1 and 5.3).

5.1 Calibration Tests

Before proceeding to the performance tests, it is necessary to define a corrective-curve due to the parasite-forces generated by the pressurised flexible-tubes. The magnitude of such correction depends on the pressure of the feed-line w.r.t. the external pressure, defined as $\Delta p = p_c - p_a$. Additionally, further corrections come from the calibration of the load-cell, by verifying variations of sensor's characteristics (SLOPE $[N/A]$) from fabric-settings. The total-correction on thrust-measurements by the DAQ is expressed by the following:

$$F[N] = \text{SLOPE}\,[N/A] \cdot (F[A] - a\,\Delta p^2 - b\,\Delta p - \text{OFFSET}[A]) \tag{7}$$

where a and b are coefficients of a 2nd-grade polynomial curve derived from calibration-tests and change between near-vacuum and sea-level environment, while OFFSET$[A]$ is the off-set at the beginning of each test so to cancel-out any pre-loads on the sensor (here set as null/compressive due to the arrangement of the setup). The maximum correction applies at near-vacuum conditions (where the effect of parasite-forces is higher as the flexible-tubes expand in a low-pressure environment) and never exceeds a $\Delta F\,[A] = 4 \times 10^{-5}\,A$ (corresponding to c.a $0.5\,N$). This result was achieved through an accurate location and shortening of the section-of-influence of the tubes on the final setup. Instead, the correction at sea-level results in the range of the measurement error of the sensor (below $0.1\,N$).

Last element left to discuss of Eq. 7 is the SLOPE $[N/A]$, namely *load-cell characteristics*, which could vary with time from the original fabric-settings by the provider. This is mainly due to sensor-integration on the final-setup, together with degradation of its response due to multiple uses during the tests (see Figure 6). As noticeable from Figure 6b, the sensor correctly operates in a linear-response interval. Nevertheless, its characteristics changed (it increased, meaning that on the sensor the same applied-load is translated to higher amperage w.r.t. to Figure 6a). The exact reasons for this are not yet clear (as mentioned, it could be due to sensor-integration on the setup, or more plausibly to sensor-degradation during usage, due to vibrations during tests with active free-streams). Nevertheless, the process has been monitored carefully and its impact on the measurements embed through a linear correction via a dedicated *corrective-factor* ($SLOPE_{calibration}/SLOPE_{fabric}$) that accounts for any gain-deviations between experiments and fabric-settings. Further discrepancies from the original SLOPE, up to loss of linearity or strong hysteresis, surely imply a substitution of the load-cell (this was the case during the tests on DB nozzle). Generally, this can be verified through the analysis of repeatability of results for performance tests (see Section 5.2).

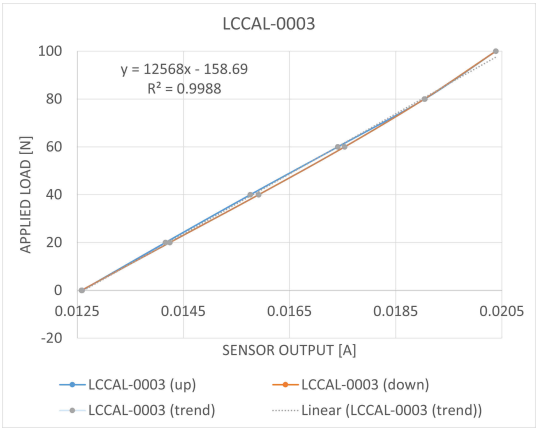

(a) Sensor's Characteristics before setup-adaptation.

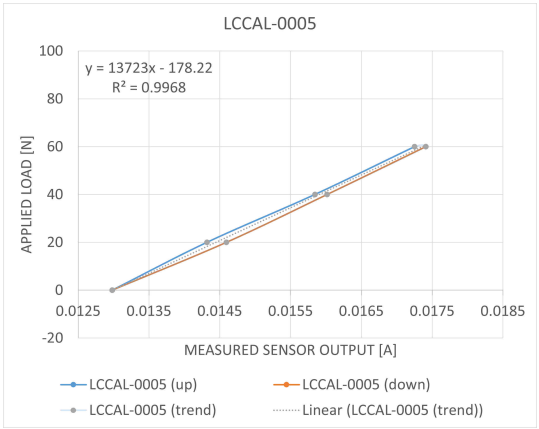

(b) Sensor's Characteristics after setup-adaptation.

Figure 6: Verification of characteristics of the load-cell (i.e., SLOPE $[N/A]$) before and after the adaptation of the setup.

DOI: 10.13009/EUCASS2023-638

5.2 Performance Tests

This section is dedicated to test campaigns that deliver the nozzles performance at specific *NPR*s of interest in absence of free-streams. More specifically, the nozzles are tested in "static-fire" (on-design steady-state conditions in the pressure-chamber, see Table 1) but at different ambient conditions (p_{amb}). The performance obtained for all the nozzles are reported in Figure 7. As the measurements of each experiment are averaged over 1 *s* intervals and over a minimum of three tests per NPR-of-interest, the *standard deviation* reported in Figure 7 is an indicator of the reproducibility of the results. These values are subsequently scaled if the experimental condition deviates from the *NPR* target (within a maximum of $\Delta NPR = \pm 2.0$). Further details on this scaling procedure can be found in Section 5.3.

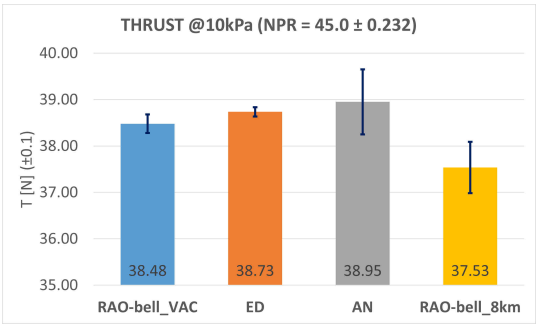

(a) Thrust (T) at $NPR = 45.0$.

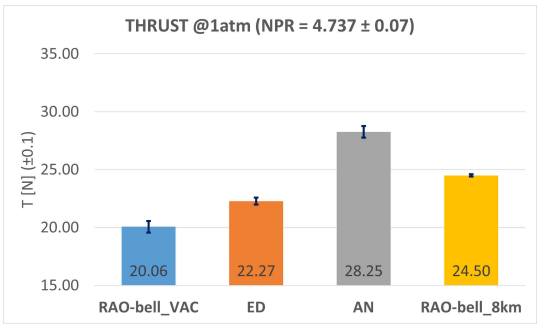

(b) Thrust (T) at $NPR = 4.737$.

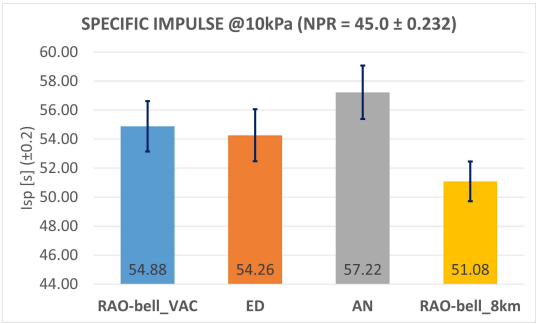

(c) Specific Impulse (I_{sp}) at $NPR = 45.0$.

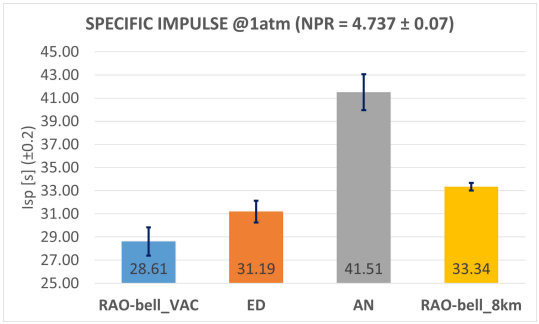

(d) Specific Impulse (I_{sp}) at $NPR = 4.737$.

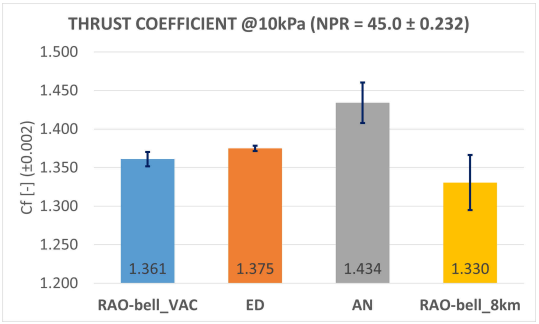

(e) Nozzle Thrust Coefficient (C_f) at $NPR = 45.0$.

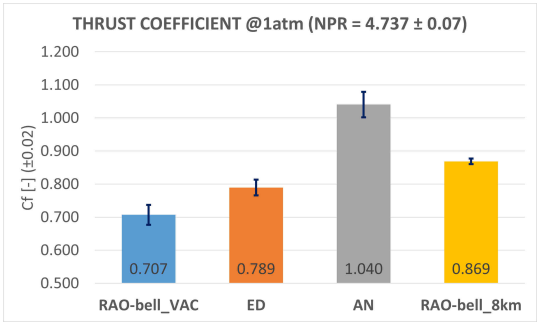

(f) Nozzle Thrust Coefficient (C_f) at $NPR = 4.737$.

Figure 7: Comparison on performance (*averaged* & *scaled*) between the different nozzle models at ANC's design-point ($NPR = 45.0$) and SLS ($NPR = 4.737$).

In Figure 8, the BOS pictures at *NPRs* of interest are available. The results in both Figure 7 and Figure 8 are discussed in detail within the dedicated Section 7.1. In particular, the quantitative results here reported are analysed in terms of performance-gains between the different models and losses w.r.t. their respective ideal-case.

DOI: 10.13009/EUCASS2023-638

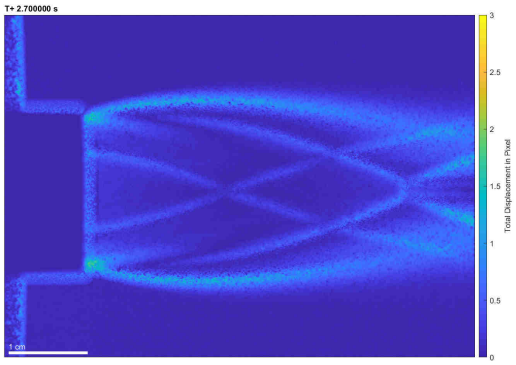

(a) *RAO-bell_VAC* nozzle at NPR = 45.0 (DP).

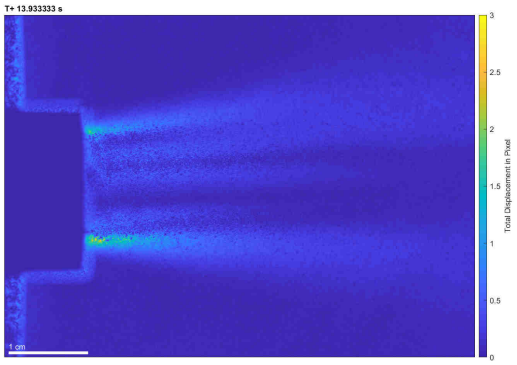

(b) *RAO-bell_VAC* nozzle at NPR = 4.737.

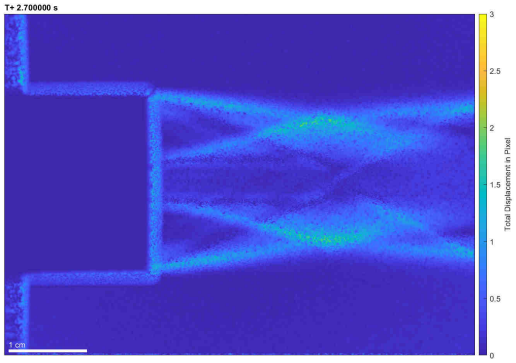

(c) *ED* nozzle at NPR = 45.0.

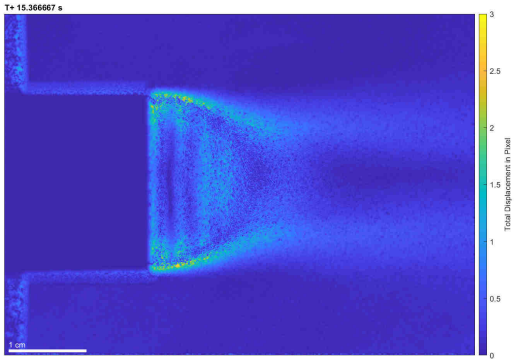

(d) *ED* nozzle at NPR = 4.737.

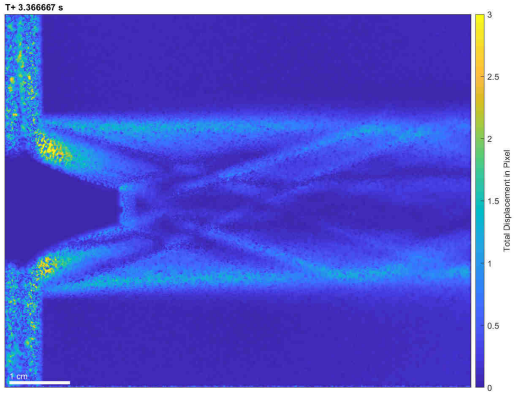

(e) *AN* nozzle at NPR = 45.0 (DP).

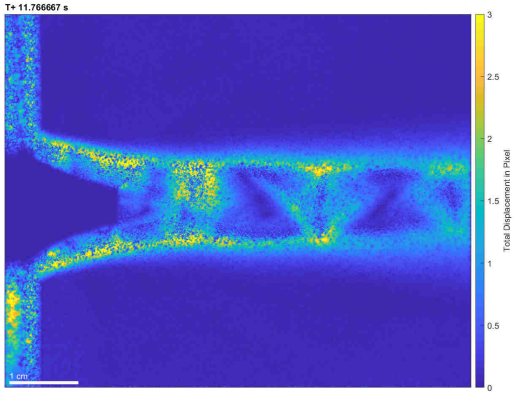

(f) *AN* nozzle at NPR = 4.737.

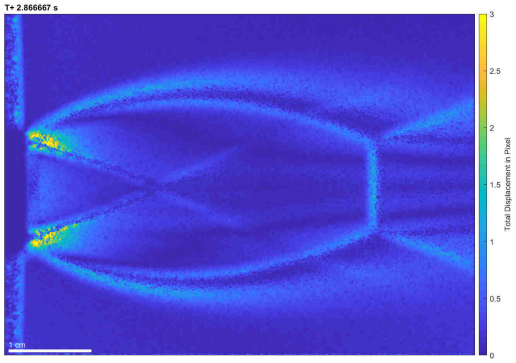

(g) *RAO-bell_8KM* nozzle at NPR = 45.0.

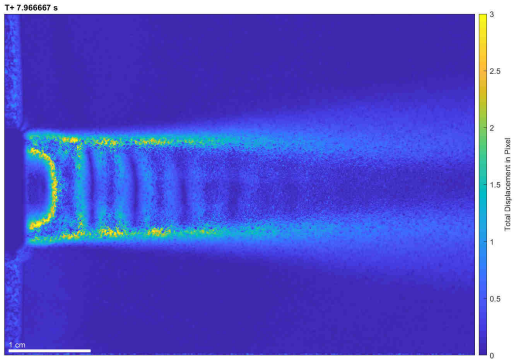

(h) *RAO-bell_8KM* nozzle at NPR = 4.737.

Figure 8: Background-Oriented Schlieren (BOS) outputs from *Performance Curves* tests.

DOI: 10.13009/EUCASS2023-638

5.3 Performance Curves Tests

This test campaigns delivers the NPR-Thrust characteristics for each nozzle, through a series of sub-tests at variable ambient-pressure and constant chamber-conditions. The reasons for this come as: a qualitative visualisation tool of the individual behaviour of each nozzle, including altitude-adaptive characteristics; method to scale the experimental results of performance-tests to their NPR target (NPR_{ref}) through a corrective-factor, depending on the deviation of the experimental NPR (NPR_{exp}) from the original target value during the experiment. By this solution, it is possible to evaluate a *corrected-thrust* value (T_{corr}) also for NPRs not exactly correspondent to the target value (but still close). This situation could happen quite often during tests at SLS or in counter-flow/retro-flow configurations, where it is more challenging to control the ambient conditions. Of course, such corrections have limits of validity, estimated on sensor-accuracy and repeatability of the experiments (confidently, within a maximum $\Delta NPR = NPR_{exp} - NPR_{ref} = \pm 2.0$).

The interval of interest for the performance-curves starts from the design-point of ANC's and *RAO-Bell_VAC*, then down to SLS ($NPR = 4.737 \div 45.0$). It is divided in four sub-intervals in order to always operate at steady-state. This comes as the compressed-air tank cannot provide a constant chamber-pressure during a single-run along the entire span-of-interest of NPR. Then, the data acquired during these tests is extracted in its steady-state interval, then merged and plotted against the corresponding NPR. A clarifying example for the RAO-Bell is provided in Figure 9.

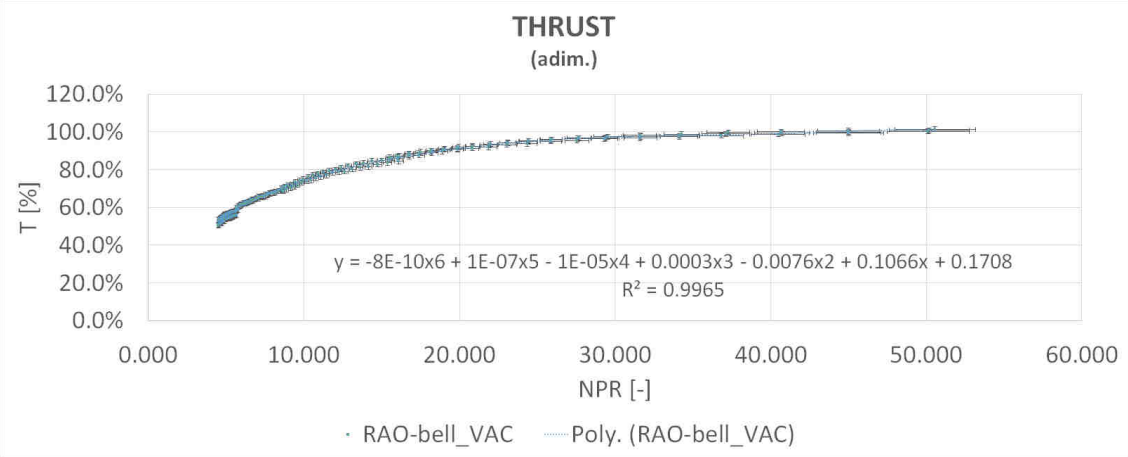

Figure 9: Example of experimental *Performance Curve* (here, normalised Thrust T for a RAO-Bell nozzle designed for vacuum operations).

The performance curves are derived for T, I_{sp} and C_F (refer Section 2), and are always reported in dimensionless terms (e.g., normalised thrust, in case of Figure 9). This is obtained by dividing the experimental values by their maximum average-value ($NPR = 45.0$) obtained during the performance-curve campaign for each nozzle, as this approach preserves the validity of the curves despite of small deviations over their maximum-values). Then, it is derived for each curve a 6th-grade polynomial and their coefficients are used to correct the performance (refer Section 5.2). This procedure applies to each nozzle, depending on its own curve respectively. The correction of the experimental thrust follows Eq. 8:

$$T_{corr} = T(NPR_{ref}) = T_{exp} + \sum_{k=1}^{N=6} c_k \left(NPR_{ref}^k - NPR_{exp}^k\right) \tag{8}$$

where T_{corr} is the final value searched for the NPR_{ref} (e.g., $NPR = 4.737$ at SLS for a $p_c = 4.8\,bar$), while T_{exp} and NPR_{exp} are the Thrust and NPR measured during the experiments, respectively. An equivalent procedure applies also to specific-impulse and thrust-coefficient. As for the performance-tests, the *standard deviation* is a measure of the reproducibility of the tests and their results. By following this approach, it is still possible to have a realistic prediction of the performance at any target NPR, based on experimental-data and numeric-correction within the interval of confidence specified.

DOI: 10.13009/EUCASS2023-638

6. Retro-propulsion Campaign

This series of tests aims to characterise the aerodynamic response of the extended body while invested by a subsonic free-stream, through a combination of counter-flow and retro-flow tests, together with earlier results from the performance-evaluation campaign (refer Section 5). The reference condition chosen for this campaign takes into account the methodology proposed by Nonaka et al.[9] to define the combination of ambient conditions, free-stream regimes and relative distance (d) between counter-flow nozzle and baseplate. Additional scaling factors from Korzun et al.[10] are also considered for this study (further details on these are not reported in this manuscript, but can be found in the referenced publication). Ultimately, the aerodynamics of a real-case landing-burn and of a retro-flow experiment are comparable in case that the following parameters coincide:

- Mach and Reynolds numbers of both the nozzle-jet at the exit-area and of the free-stream (M_j, M_∞, Re_j, Re_∞);
- ratio of the nozzle-exit-pressure to the atmospheric-pressure (p_e/p_{amb});
- scaling parameters for gas-species of the jet (γ_j, $MW_j\,T_{j,0}$) and free-stream (γ_∞, $MW_\infty\,T_{\infty,0}$);
- ratio of mass-flow of the jet ($\rho_j\,v_j\,A_e$) to the free-stream mass-flow ($\rho_\infty\,v_\infty\,A_B$);
- ratio of the momentum-flux of the jet ($f_j = \rho_j\,v_j^2\,A_e$) to the free-stream momentum-flux ($f_\infty = \rho_\infty\,v_\infty^2\,A_B$);

It is due noticing that the latter (namely, *momentum-flux-ratio*) could be alternatively described in terms of C_T[10], which is more suitable for studies on advanced nozzles to include the effects of altitude-compensation.

In order to realise a satisfying study in Mach and Reynolds analogy, the M_j and Re_∞ should be as close as possible to the real-case[9]. Nevertheless, it is clear that the limitations of the test-bench, due to the cold-gas and the lower free-stream velocities, pone some insurmountable technical-limitations. In particular, the Re_∞ results at least one order of magnitude lower than in the real-case, while the M_j for cold-gas could barely reach 2.5 at these expansion-ratios (higher values could generate condensation, in absence of pre-heating of the gas). Nevertheless, as suggested by Nonaka et al.[9], in order to achieve a comprehensive flow-structure around the testing model that results comparable to the real-case, it is sufficient that the Re_∞ is high enough to ensure turbulent-flow on the body (as in the real-case, but with larger vortex-structures) and the separation-point resulting fixed at the edge of the baseplate. This was duly verified through CFD studies[15] (see Figure 16a). Therefore, by adopting a Mach analogy in terms of M_j/M_∞ ratio (instead of M_j, as suggested by Nonaka et al.[9]), the experimental results can still include information useful to understand at qualitatively level the characterization of the aerodynamic force acting on the body in retro-flow configurations.

As reference real-case, the *Falcon 9 - Block 5 (NROL-85)* mission is chosen (single-engine, 80% throttling, 2.34 oxidiser/fuel ratio), in correspondence of a trajectory-point at $u_\infty \approx 80\,m/s$ during its landing-burn. The scaling-parameters for this case are numerically estimated from available telemetry-data[20] and various simulations through *Rocket Propulsion Analysis*© tool. Instead, for the test-case the parameters for the experiments are evaluated preliminarily as ideal values for the reference RAO-bell nozzle designed for near-SLS operations, derived analytically in hypothesis of isoentropic nozzle-flow[11]. Eventually, a trade-off between different combinations of p_{amb}, u_0 and d led to a choice of $u_{x=d} \equiv u(d,0) = 60\,m/s$ (at $p_a = 1\,atm$) as a good compromise between comparability of results and practicality of the experiments. A summary of the parameters for such combinations are available in Table 2.

Table 2: Comparison between real-case and test-case, based on ambient/free-stream-conditions, gas properties and other scaling parameters.

	NROL-85[a]	**Test-case**[b]	Δ[%]
p_e/p_{amb}	0.342	0.342	0.0%
M_j	3.915	2.366	−40.3%
M_j/M_∞	15.938	13.490	−15.4%
γ_j	1.250	1.400	+12.0%
$\rho_j\,v_j\,A_e/\rho_\infty\,v_\infty\,A_B$	0.189	0.103	−45.5%
f_j/f_∞	7.164	0.995	−86.1%
C_T	14.921	1.441	−90.3%
$MW_j\,T_{j,0}/MW_\infty\,T_{\infty,0}$	10.053	0.996	−90.1%

A more detailed discussion on the high deviations from the real-case (Δ) in Table 2 are provided in Section 8, together with additional aspects/limitations for the chosen test-configuration and foreseeable improvements.

DOI: 10.13009/EUCASS2023-638

6.1 Counter-flow Tests

This series of tests delivers the aerodynamic performance of the extended body in presence of an $u_{x=d} \equiv u(d,0)$ equal to 60 m/s. Alternatively, this corresponds to a $M_{x=d} \equiv M(d,0) = 0.175$ for the same air-speed at the baseplate in SLS conditions. In order to maintain the desired $u_{x=d}$ at the baseplate, the u_0 varies for each $d = 500mm, 550mm, 600mm$ according to the methodology adopted in Section 4. The results are provided in terms of C_D in Figure 10.

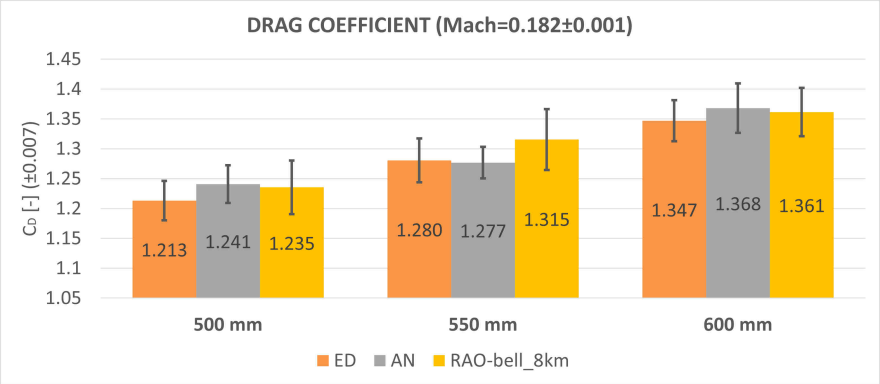

Figure 10: Experimental results on drag-coefficient (C_D) of the extended body in *counter-flow* scenario, while invested by a subsonic conical free-stream at $M_{x=d} = 0.182$.

Due to notice that the standard-deviation in Figure 10 provides information on the repeatability of the tests. Unfortunately, this category of test provides the higher dispersion, due to the strong vibrations induced by turbulence on the setup and, in general, a very high sensitivity to the evolution of the macro-vortexes structures at the shear-layer of the conical flow. A more detailed analysis of results is provided in Section 7.

6.2 Retro-flow Tests

This series of tests delivers the performance of the different nozzle-models and the aerodynamic performance of the extended body in a retro-flow configuration ($M(d,0) = 0.175$ in SLS for the same air-speed). The $d = 500mm$ has been excluded after a pre-evaluation on the minimum distance from the free-stream nozzle in order to avoid any impingement of the counter-flow in the pre-chamber[19].

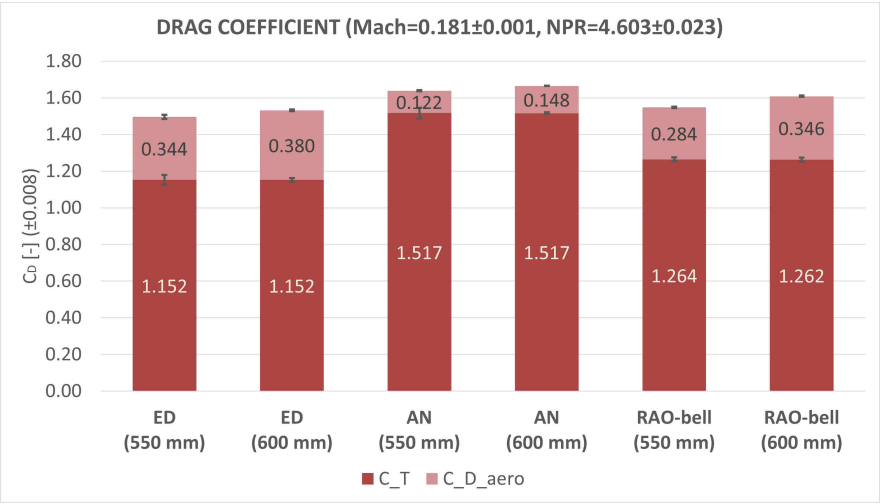

Figure 11: Experimental results on drag-coefficient (C_D) of the extended body in *retro-flow* scenario, while invested by a subsonic conical free-stream at $M_{x=d} = 0.181$.

The T_{corr} from *performance-tests* (refer Section 5.2) is scaled to the NPR of the retro-flow experiments in agreement with Eq. 7, then adopted to evaluate the C_T and $C_{D_{aero}}$ contributions. Again, the standard-deviation in Figure 11 provides information on the repeatability of the tests. A detailed description of the results is provided in Section 7.

DOI: 10.13009/EUCASS2023-638

7. Discussion of Results

This section reviews the results of the experimental campaigns for nozzle performance and aerodynamic performance in static-fire and counter-flow/retro-flow configurations, here reported in Section 7.1 and Section 7.2, respectively. Additionally, in Section 7.3, more insights are provided on the interactions with parallel CFD studies for both the design-process of the setup and definition of the test-procedures, together with preliminary results from CFD that offer insights and suggest further improvements for research activities to follow.

7.1 Discussion of Performance Results

Before providing a discussion of the results presented in Section 5, the design of the nozzles w.r.t. their expected performance from analytic calculation is verified at both design-point and SLS. It is reported in Table 3 and Table 4 by following the definitions of *performance-correction-factors* (alternatively, *efficiencies*) as provided by Sutton et al.[11].

Table 3: Verification of performance at Design Point (losses w.r.t. *1D-Ideal-Case* of each nozzle, ideal-values are derived analytically in hypothesis of isoentropic nozzle-flow[11]).

	$\zeta_F = T/T_i$	I_{sp}/I_{sp_i}	C_F/C_{F_i}	[a] $\zeta_d = \dot{m}/\dot{m}_i$	[b] $\zeta_v = v_e/v_{e_i}$
RAO-bell_VAC	0.924	0.870	0.923	1.001	0.923
ED	0.930	0.860	0.932	0.993	0.937
AS	0.936	0.907	0.972	0.949	0.985
RAO-bell_8KM [c]	0.913	0.820	0.913	1.042	0.876

[a] Expected $\zeta_d > 1$ for real-case.
[b] $\zeta_v = \sqrt{e} = \zeta_F/\zeta_d$.[11]
[c] $NPR_{o.d.} = 13.852$, $\varepsilon = 2.328$.

From the analysis at design point, the three nozzles designed at near-vacuum ($NPR_{o.d.} = 45.0$) lose between 6.4 % and 7.6 % of their ideal-thrust, while the *RAO-bell_8KM* ($NPR_{o.d.} = 13.852$) goes down c.a 8.7 %. This behaviour can be easily explained: the 3D-printing process in polymeric-resins has a resolution limit of 25 μm per layer, which can be minimised by increasing the printing-angle. The latter is the user-defined orientation of the model w.r.t. the printing-plane. In particular, the printing resolution increases if the same contour is distributed through a higher-number of layers by changing this angle. Inevitably, the printing-process can generate deviations from the original contour, thus incomplete expansion, higher viscous-effects and divergence/a-symmetry of the flow. In particular, this effect for AN is enhanced (see Figure 8e, 8f). As the specimens are printed as a single piece, the printing at not-null angles could result in the central bodies (i.e., spike or pintle for AN and ED nozzle) to lose their axial-symmetry to some extent due to gravity. In general, these deviations from the original contour are limited at high *NPRs*, while they become more evident in case of high over-expansion as the flow tends to separate earlier in presence of imperfections, sometimes causing a-symmetric flow-deviations as for the *RAO-bell_VAC* at SLS (see Figure 8b). Moreover, liquid droplets (e.g., moisture or condensation) in cold-flows can also reduce the performance, even though such phenomena do not appear from the BOS pictures (see Figure 8). Overall, the close gap in losses between all the nozzles designed for near-vacuum exclude that the lower performance constitute a case of incorrect design (even though the nozzles could always be further thrust-optimised), while for the specific case of the *RAO-bell_8KM* the higher losses (still within a 10 % total margin) suggest that the design of its contour might be improved by reducing the exit-angle at the throat[11] ($\theta_i < 30^o$), at cost of a longer nozzle.

Then, the verification process proceeds for SLS conditions, with the exclusion of the RAO-bell nozzles (as both of them experience flow-separation according to Summerfield-criterion[21]). It is due noticing that the ideal-case for the ANCs considers an "optimum-adaptation" to the ambient pressure ($p_{e_i} = p_{amb}$)[11], which is quite plausible to be an over-estimation for any real-case, even with the best design achievable. Nevertheless, previous analyses[6] showed that c.a 50 % of pressure-compensation already provides more than 90 % of the performance-gains achievable by the adaptation to ambience. From this preliminary verification, it is already clear that the AN surpasses with no doubts the ED in terms of efficiency at SLS, thus verifying the sensitivity of the ED nozzle-concept to the effects of wake-evacuation (or *aspiration-drag*)[18]. Interestingly, the aerospike achieves a higher efficiency also w.r.t. the on-design case in Table 3, suggesting that the adaptation along the spike might reduce some divergence losses (see Figure 8f).

DOI: 10.13009/EUCASS2023-638

Table 4: Verification of performance at SLS (losses w.r.t. respective *1D-Ideal-Case*, ideal-values are derived analytically in hypothesis of isoentropic nozzle-flow[11]).

	$\zeta_F = T/T_i$	I_{sp}/I_{sp_i}	C_F/C_{F_i}	[a] $\zeta_d = \dot{m}/\dot{m}_i$	[b] $\zeta_v = v_e/v_{e_i}$
ED	0.745	0.672	0.727	1.049	0.710
AS	0.945	0.894	0.959	0.996	0.949

[a] Expected $\zeta_d > 1$ for real-case.
[b] $\zeta_v = \sqrt{e} = \zeta_F/\zeta_d$[11].

The final step is to proceed with a direct comparison of the nozzle performance between the specimens designed for near-vacuum (ANCs and *RAO-bell_VAC*) and the nozzle designed for near-SLS operations (*RAO-bell_8KM*). An overview is provided in Table 5. The behaviour of the conventional nozzles is in agreement with the basics of nozzle-theory[11]: the *RAO-bell_VAC* performs better than *RAO-bell_8KM* at $NPR = 45.0$ (only +2.5 % in thrust for an ε that doubles the one of *RAO-bell_8KM*, but almost +7.5 % in I_{sp}), while at SLS the unavoidable flow-separation dramatically compromises its flow-expansion. In this case, additional losses are addressable to asymmetric flow-development for low *NPRs* (see Figure 8b). On contrary, the ANCs preserve a relatively high-thrust at SLS ($NPR = 4.737$) despite of their high expansion-ratios, with the aerospike outperforming all the other nozzles with a +15.3 % (value in perfect agreement with literature[1,11,17,22]). Curiously, the ED nozzle fits right in between the two conventional nozzles in terms of thrust at SLS, thus under-performing w.r.t. the *RAO-bell_8KM*. At near-vacuum ($NPR = 45.0$), both the ANCs offer higher performance than the *RAO-bell_VAC* despite of sharing identical chamber-parameters and design-point. One plausible explanation is that both the C. C. Lee and Angelino's design-methods, for AN and ED respectively, as based on ideal-contouring, might reduce the impact of viscous-losses. In the case of the ED nozzle, this comes with a longer nozzle, but for the AN (truncation at 45 % of ideal-length) the form-factor is less penalising than for the ED, thus providing higher performance at a reduced volumetric-encumbrance. Moreover, a +24 % of I_{sp} implies higher efficiency and far-less propellant-consumption, not to mention that by including a base-bleed (1-2 % of the total mass-flow) the performance-gains could increase even more[17]. The AN exhibits an asymmetric flow in both ambient conditions (see Figures 8e and 8f) for the reasons addressed before in this section, suggesting that an optimisation of the printing angle (alternatively, lightening of the spike) could increase the performance further.

Table 5: Performance comparison w.r.t. *RAO-bell_8KM* operating at same *NPR*.

	NPR_{ref}	ΔF	ΔI_{sp}	ΔC_F
RAO-bell_VAC [a]	45.000	2.5 %	7.4 %	2.29 %
RAO-bell_VAC	4.737	-18.1 %	-14.2 %	-18.61 %
ED [a]	45.000	3.2 %	6.2 %	3.34 %
ED	4.737	-9.1 %	-6.4 %	-9.12 %
AS [a]	45.000	3.8 %	12.0 %	7.79 %
AS	4.737	15.3 %	24.5 %	19.78 %

[a] Design-point ($NPR_{o.d.} = 45.0$).

In closure, more details (so far, not yet addressed) come from the BOS pictures (see Figure 8): the nozzles designed for near-vacuum operate close to an optimum expansion, with the exception of the ED nozzle that results slightly over-expanded. This is a consequence of the higher expansion-ratio, that was a deliberate design choice to limit the impact on performance of the reduced effective exit-area due to the presence of the pintle. The presence of internal-shocks for the *RAO-bell_VAC* at near-vacuum (see Figure 8a) is a consequence of its parabolic-contour. On contrary, at near-vacuum the *RAO-bell_8KM* operates highly under-expanded, this is clearly depicted by the diverge of the flow at the nozzle-exit (see Figure 8g) and is a consequence of its smaller expansion-ratio. This nozzle exhibits over-expansion at SLS but no flow-separation, as originally intended by design. Further details on the BOS analysis will be delivered in future publications in comparison with validated outcomes from the CFD studies.

7.2 Discussion of Counter-flow/Retro-flow Results

In the following section, the outcomes of counter-flow and retro-flow experiments reported in Section 6.1 and 6.2 are discussed. In particular, the results provided in Figure 10 are plotted here in Figure 12 in function of the normalised distance (d/D) of the baseplate from the nozzle of the free-stream (where $D = 100.0\,mm$ is the diameter of such nozzle). From the results reported in Figure 10, the extended body exhibits a higher aerodynamic-drag for longer distances

DOI: 10.13009/EUCASS2023-638

(note that the Mach number at the baseplate, or $M_{x=d}$, does not change between the tests at different d/D), due to the development of the conical free-stream towards a full-turbulent regime (refer Figure 4). In general, a turbulent free-stream is closer to a realistic case-study of a VTVL-RLV[9]. Nevertheless, it is always necessary for the experiments to find a compromise on d/D, in order to: contain the nozzle-jet within the laminar-core for the retro-flow tests (closer to case-study, refer Section 2); reduce the dispersion of velocity-profiles in radial-direction due to a non-uniform distribution (refer Section 4). The last point emerges from the development of conical-flows in still-ambience and it constitutes a feature of the TUD vacuum-wind-tunnel that at current state cannot be avoided (refer Section 4 for clarifications). In particular, such dependency is more visible in Figure 12. This is addressed to the variation of the radial-distribution of $u_{x,y}$ and $Re_{x,y}$, in hypothesis of axial-symmetric flow and for identical $M_{x=d}$ at various d/D (different u_0 values[5,14]).

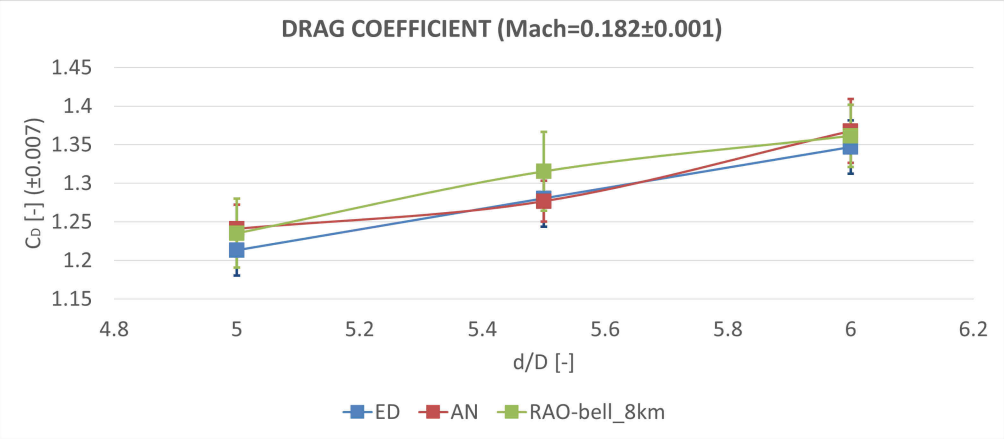

Figure 12: Experimental results on drag-coefficient (C_D) w.r.t. normalised distance (d/D) of the extended body in *counter-flow* scenario, while invested by a subsonic conical free-stream at $M_{x=d} = 0.182$.

As the $M_{x=d}$ does not change for different d/D, the only contribution that could influence the differences in C_D and its behaviour with d/D is the form-factor of each nozzle for different $Re_{x,y}$ over the extended body. In particular, the ED nozzle offers the widest exit-area, while the aerospike reduces the stagnation of the free-stream to the baseplate thanks to its peculiar geometry (a higher average-velocity at the baseplate-tip is verified numerically[15]). It is quite plausible that such tendency would reduce asymptotically once that the extended body is invested by a fully-developed turbulent free-stream for $x/D > 7.0$. Nevertheless, it is quite interesting to quantify how different nozzle-types behave differently for higher $Re_{x,y}$ distributions, depending on their form-factor. In particular, for applications to RLVs of aerospike engines at high expansion-ratios, this effect could strongly affect the aerodynamics (thus, vehicle stability) of the RLV during an aerodynamic descent, due to the additional viscous-drag along the spike and the higher stream-velocity at the baseplate[2]. More research in this regard could be pursued for different combinations of ε an truncation-lengths for ANs at various $M_{x=d}$ (consequently, different $Re_{x,y}$ distributions over the extended body).

Further discussions involve the results presented in Section 6.2 (see Figure 11) on the impact of retro-propulsion on the total-drag. As expected, the contribution of the aerodynamic-thrust-coefficient (C_T) to the total-drag is dominant w.r.t. the residual aerodynamic-drag ($C_{D_{aero}}$), even though the increments in total-drag are strongly limited due to the low-thrust w.r.t. the dynamic pressure ($1.15 < C_T < 1.52$). In order to better visualise this result, in Figure 13 are reported the individual contributions to the total-drag, reviewed in terms of increment/decrement of the aerodynamic-drag-coefficients (namely, ΔC_D for total-drag and $\Delta C_{D_{aero}}$ for aerodynamic-drag). The dramatic drop in the contribution of the aerodynamic-drag suggests that the counter-flow is strongly altered by the nozzle-jet. Unfortunately, there is not a definitive way to verify if this reflects a collateral effect of operating with a conical counter-flow (instead of a uniform one), but comparatives from literature can offer some additional insights: in general, the experimental $C_{D_{aero}}$ always drops by 75 % (up to an order of magnitude for $C_T > 1.5$), in agreement with Nonaka et al.[9] for comparable M_j and f_j/f_∞. This confirms a strong dependency from these parameters, while the dependency from p_e/p_{amb} (as for supersonic-retro-propulsion[10]) seems strongly reduced in subsonic retro-flows. An additional confirmation for $C_T > 1.5$ comes from a real case-study on a RLV model (RETALT1, refer Marwege et al.[23]), as the $C_{D_{aero}}$ exhibits a 90 % drop for $M_\infty = 0.5$ and $C_T = 3.34$. Though, in this specific case the comparative comes only on a qualitative level, as the tests on the RLV model adopts hot-gas and a much higher M_j. Nevertheless, the correlation between $C_{D_{aero}}$ and C_T (better highlighted in Figure 15) encourage the results obtained through the proposed methodology.

DOI: 10.13009/EUCASS2023-638

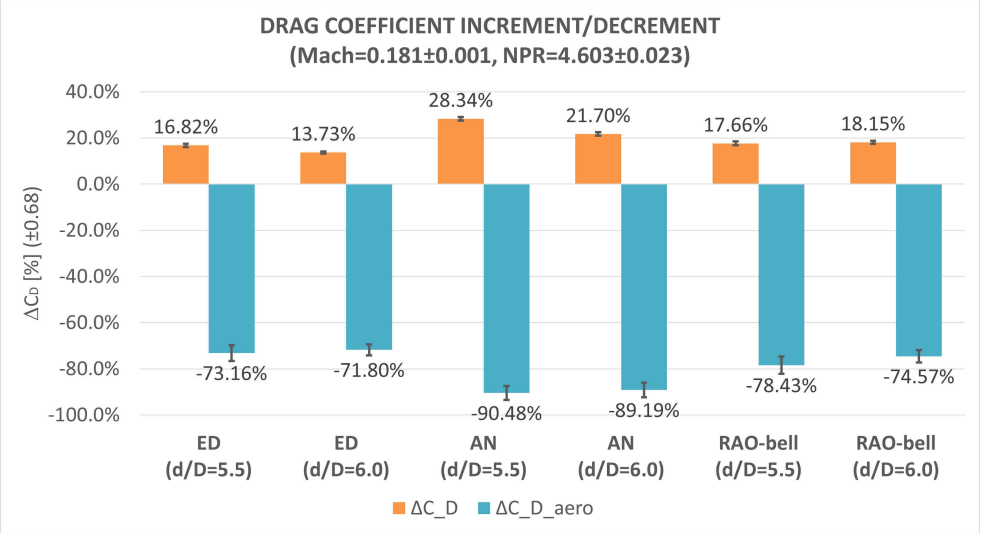

Figure 13: Experimental results on increment/decrement of drag-coefficients (ΔC_D, $\Delta C_{D_{aero}}$) of the extended body in *retro-flow* scenario for $NPR = 4.603$ (invested by a subsonic conical free-stream at $M_{x=d} = 0.181$).

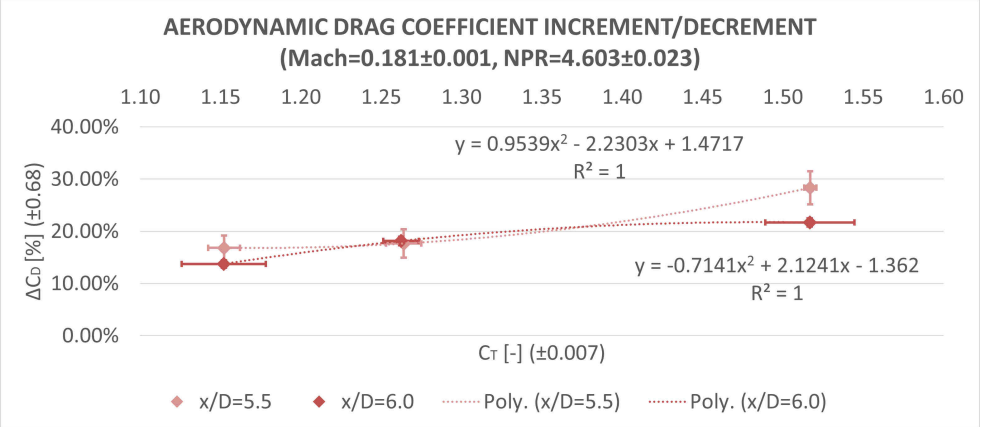

Figure 14: Increment/decrement of drag-coefficient (ΔC_D) of the extended body w.r.t. aerodynamic-thrust-coefficient (C_T) in *retro-flow* scenario for $NPR = 4.603$ (invested by a subsonic conical free-stream at $M_{x=d} = 0.181$).

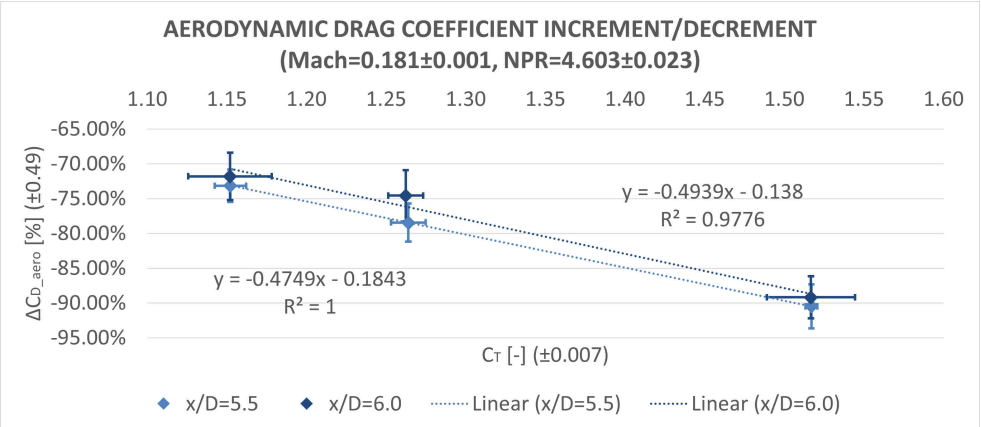

Figure 15: Increment/decrement of aerodynamic-drag-coefficient ($\Delta C_{D_{aero}}$) of the extended body w.r.t. aerodynamic-thrust-coefficient (C_T) in *retro-flow* scenario for $NPR = 4.603$ (subsonic conical free-stream at $M_{x=d} = 0.181$).

DOI: 10.13009/EUCASS2023-638

In Figure 14 it is offered an overview on the variation of total-drag (ΔC_D) depending on C_T. In general, all nozzles exhibit an increment in total-drag that increases with C_T at the same $M_{x=d}$. In particular, the AN exhibits the highest increment as it also presents the highest thrust at SLS. Curiously, the effect of the $Re_{x,y}$ on the extended body inverts the second-derivative of the fitting curves. Further analysis in this regard might be of interest. In closure, a final comment regards the dependency of $\Delta C_{D_{aero}}$ on C_T and, more specifically, in Figure 15 it is shown a linear dependency on this latter, which is not necessarily the case for any subsonic counter-flow (refer Nonaka et al.[9]). Nevertheless, such behaviour finds similarities with the scaling of the normalized bow-shock height with the square root of the momentum ratio (case $1.0 < \sqrt{C_T} < 2.0$) for studies on supersonic retro-propulsion[10,24].

7.3 Preliminary Results from CFD Simulations

The role of CFD simulations for the methodology of investigation, definition of test-procedures and comparative on results, constitutes an important element for the retro-flow experiments with subsonic free-streams, as the BOS visualisation cannot provide information on the flow-topology of the AI region. Additionally, it provided information on the distance of reattachment point of the free-stream in both counter-flow and retro-flow experiments, in order to size the body-extension[15]. Further details on the validation of CFD models are delegated to future publications. Nevertheless, some useful insights can be provided to the reader. Preliminary results on the nozzle performance in retro-flow configuration show a common behaviour between the models: the local static-pressure (at nozzle-exit) is lower than the p_{amb} without counter-flows, as the the nozzle-jet expands in an low-pressure AI region that partially presents a not-null velocity (stagnation conditions only at the baseplate, see Figure 16). In general, this results in a +2 % in the effective NPR and a +1 % in the nozzle performance (higher for ED) as the nozzles perform in a better adapted operating condition than in absence of counter-flows. This result is presented in Table 6 and further details will be provided in a following publication. For the interest of the experimental activities, if such effect is confirmed after the validation of CFD models, it might be necessary to update the effective NPR in retro-flow configurations.

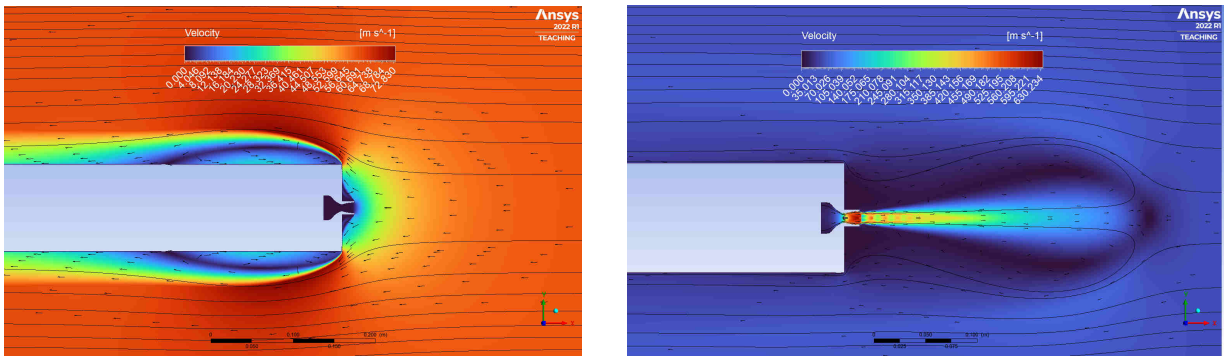

(a) Counter-flow at SLS (uniform free-stream).

(b) Retro-flow at SLS (uniform free-stream).

Figure 16: CFD post-processing of velocity-profiles for *RAO-bell_8KM* nozzle in counter-flow and retro-flow configurations ($NRP = 4.737, u_\infty = 60.0\,m/s$)[15].

Table 6: CFD preliminary-results on variation of nozzles performance between *static-fire* and *retro-flow* configurations at SLS ($NPR = 4.737$)[15].

	F_x	C_F	I_{sp}	NPR
ED[a]	+2.22 %	+2.26 %	+2.26 %	+2.07 %
AS[a]	+0.82 %	+0.84 %	+0.84 %	+2.13 %
RAO-bell_8k[a]	+0.98 %	+1.02 %	+1.11 %	+2.18 %

[a] The indicated values refer to a uniform asymptotic free-stream.

As mentioned, the CFD constitutes also a visualisation tool for the AI region, which allows to correlate the distance of the stagnation-point (AI-region extension) to the C_T (alternatively, to momentum-flux-ratio f_j/f_∞). More studies will follow on the dependency of the penetration of nozzle-jets in subsonic counter-flows on this parameters, based on the methodology provided by Jarvinen et al.[25,26] .

DOI: 10.13009/EUCASS2023-638

8. Limitations & Outlook

In general, the proposed methodology provides outcomes in good agreement with results already available in literature (refer Section 7). Additionally, the presence of the laminar-core (verified in Section 4) ensures a flow-field compatibility of AI-region between experiments in conical-flow and CFD in uniform-flow. Unfortunately, the same cannot be said for the aerodynamic performance on the extended body, as the test-bench inherits important limitations from the conical-flow. Further improvements could envisage the adoption of a wind-tunnel for uniform-flows. Moreover, solutions to reduce the parasite aerodynamic drag of the support-structure of the setup are envisaged, as well as the integration of characteristic geometries designed for VTVL-RLVs on the body-extension, such as: clustered-nozzles (e.g., octa-web configurations as Falcon 9); 3D-printed control-surfaces (e.g., planar fins); other disturbances (e.g., landing legs). On contrary, it would be necessary to re-design the pressure-chamber in its entirety in order to increase the aspect-ratio. Nevertheless, a parametric study on the form-factors[10] (i.e., *nozzle-exit-to-baseplate*, *nozzle-throat-to-baseplate*, *aspect-ratio*) could provide additional information in this regard. In order to better achieve a precise calculation of u_0 and ρ, the temperature should be read through a dedicated sensor mounted directly inside the pre-chamber. Moreover, the pressure-probes along the body-extension (not yet investigated for this publication) could read the differential-pressure in parallel, for the evaluation of the *pressure-coefficients* $C_p(x)$ at the side-walls. This would provide useful information on the location of the reattachment-point of the free-stream and more in general of C_D.

Another foreseeable improvement involves the reduction of the propagation of measurement-errors (e.g., aerodynamic coefficients are calculated, not direct measurements) and general methods to improve the repeatability of tests (i.e., to reduce the dispersion of data between different ambient conditions). Despite of the standard-deviations on the direct measurements being relatively low (with the exception of the total-drag in counter-flow experiments, refer Section 6), the error-propagation on the derived parameters still tends to grow fast when calculating the aerodynamic coefficients (affected from both measurement-errors and not-negligible standard-deviations between tests for total-drag and dynamic-pressure). A better solution could be to de-couple the thrust from the total-drag during retro-flow experiments, by acquiring direct-measurements of the first. By such approach, the contribution to the aerodynamic-drag on the extended body (due to the viscous-drag at the side-walls and induced-drag of the aft-body) could be ignored by measuring the thrust directly at the baseplate. Thus, the introduction of a load-cell between chamber-pressure and body-extension should ensure reliable measurements of the thrust in retro-flow configuration for free-streams within incompressible-regimes. Additionally, the integration of such sensor could improve the evaluation of nozzle performance even in absence of counter-flows, as the load-cell would be placed directly behind the pressure-chamber. Nevertheless, it should be clear that such alternative setup cannot de-couple thrust and aerodynamic-drag completely (as it would be still present the contribution of aerodynamics at the baseplate), but preliminary results from CFD show that the aerodynamic-drag at the baseplate is relatively low for the scenario of interest[15]. In definitive, a plausible way to validate this methodology would be to perform tests by adopting both sensors and then comparing their results.

A final remark regards the comparability of results between the real-case (*Falcon 9 - Block 5 (NROL-85)*) and the test-case selected for the counter-flow/retro-flow experiments (refer Section 6). Indeed, this study is limited to a qualitative analysis without direct comparability of results for the description of the AI area and its flow-topology, due to some high deviations of parameters of investigation w.r.t. the real-case. More in detail, the range of momentum-flux-ratios selected for this study is c.a one order of magnitude lower than for the real-case, as well as the scaling parameter for the different gas-species. The parameter for mass conservation is closer, but still far from the best case. This are typical limitations of cold-gas experiments at low-thurst ranges. Nevertheless, the analogy achieved for p_e/p_{amb} and M_j/M_∞ ratios already provides insights for a first qualitative comparison with the real-case. Foreseeable solutions in order to increase the comparability of results include: higher expansion-ratios for the nozzles; pre-heating of the gas (also beneficial to mitigate condensation); higher thrust-levels w.r.t. the momentum of the free-stream. Additionally, other methods of comparability proposed for supersonic retro-propulsion by Marwege et al.[27] could be addressed.

A general outlook of this study envisages the investigation of step-wise altitude-compensating nozzles (e.g., DB nozzles), together with the adoption of some of the proposed improvements. Moreover, further studies on models that integrate geometries of interest for VTVL-RLVs (e.g., clustered-nozzles, landing-legs, etc.) will be considered. The most envisaged follow-up study is a comparison between an octa-web configuration and an annular-aerospike. This comes as the aerospike engines present clear advantages in terms of performance, expected to increase thanks to a combination of higher expansion-ratios and continuous altitude-compensation properties. Their application to a future class of RLVs still constitutes an enormous technical challenge, but further studies in retro-propulsive scenarios, together with advancements in manufacturing techniques, system-engineering and simulations, could fill the TRL gap with reinvigorated motivation and better achievements than in the past.

DOI: 10.13009/EUCASS2023-638

9. Conclusions

This manuscript presents a novel methodology for investigating advanced and conventional nozzles in subsonic retro-flows. The methods defined in previous publications by the research group have been extended to the analysis of the aerodynamic performance in counter-flow/retro-flow configurations. First, the behaviour of both continuous altitude-compensating nozzles (i.e., annular-aerospike and expansion-deflection nozzles) and conventional RAO-bell nozzles is provided through "static-fire" tests with cold-gas (dry-air) at ambient conditions spreading from near-vacuum to SLS. At their design point, the ANCs exhibit performance comparable to a RAO-bell designed for near-vacuum operations ($\sim 16\,km$), while preserving them during SLS-operations thanks to their intrinsic capabilities of altitude-compensation. The annular-aerospike confirms performance gains at SLS up to 15 % w.r.t. the RAO-bell designed for near-SLS ($\sim 8\,km$), thanks to a higher expansion-ratio. On the other hand, the ED nozzle presents major losses at SLS due to its known sensitivity to the wake-evacuation and, in general, low-efficiency in open-wake regime. The analysis includes the verification of the design of each nozzles: most of their losses at design-point have been addressed to viscous effects and printing imperfections. In addition, a dedicated study on aerodynamic performance of the extended body against a subsonic counter-flow for a $M_\infty < 0.2$ (incompressible-flow) is included. In the latter, a sensitive dependency on the nozzle type and Re_∞ emerged. This reveals the importance of a correct Re_∞ in order to achieve a realistic simulation of a real-case of interest and promotes further investigations on the impact of different nozzle types on aerodynamics and stability of the vehicle. In closure, the nozzle performance and aerodynamic performance studies have been extended to the retro-flow configurations (at same M_∞): the increments in total-drag are limited due to the low-thrust w.r.t. the dynamic pressure (C_T slightly above 1.0, thus limited comparability with the real-case). Nevertheless, the correlation between aerodynamic-drag and C_T results in good agreement with literature and envisages further applications of the provided methodology to nozzles and body geometries that better simulate the real-cases of VTVL-RLVs of interest.

10. Acknowledgments

This study lies within the *ASCenSIon* (*Advancing Space Access Capabilities - Reusability and Multiple Satellite Injection*) project, an Innovative Training Network (ITN) funded within H2020. Background-Oriented Schlieren (BOS) images were evaluated using *BOSVIS* software tool by Deutsches Zentrum für Luft- und Raumfahrt e.V. (DLR), developed by Dr. S. General.

References

[1] G. Hagemann, H. Immich, T. V. Nguyen, and G. E. Dumnov. Advanced rocket nozzles. *Journal of Propulsion and Power*, 14(5), September-Oktober 1998.

[2] G. Scarlatella, M. Tajmar, and C. Bach. Advanced nozzle concepts in retro-propulsion applications for reusable launch vehicle recovery: a case study. In *IAC, 72nd International Astronautical Congress*, Dubai, United Arab Emirates, October 2021.

[3] Andrea Ferrero, Antonietta Conte, Emanuele Martelli, Francesco Nasuti, and Dario Pastrone. Dual-bell nozzle for space launchers with fluidic control of transition. In *AIAA Propulsion and Energy 2021 Forum*. American Institute of Aeronautics and Astronautics, jul 2021.

[4] F. Rossi, Z. Sápi, N. Palumbo, A. Demediuk, and Miguel Ampudia. Manufacturing and hot-fire test campaign of the demop1 aerospike engine demonstrator. In *8TH EDITION OF THE SPACE PROPULSION CONFERENCE*, number 451 in SP2022, ESTORIL, PORTUGAL, May 2022.

[5] Giuseppe Scarlatella, Jan Sieder-Katzmann, Florian Roßberg, Felix Weber, Carlos T. Mancera, Daniele Bianchi, Martin Tajmar, and Christian Bach. Design and development of a cold-flow test-bench for study of advanced nozzles in subsonic counter-flows. *Aerotecnica Missili & Spazio*, may 2022.

[6] M. Gulczynski, A. Vennitti, G. Scarlatella, G. J. Dominguez Calabuig, L. Blondel-Canepari, F. Weber, C. Bach, T. Schmiel, J. Deeken, D. Bianchi, and A. Pasini. Rlv applications: challenges and benefits of novel technologies for sustainable main stages. In *IAC, 72nd International Astronautical Congress*, 2021.

[7] D. Kirchheck, A. Marwege, J. Klevanski, J. Riehmer, and A. Gülhan. Validation of wind tunnel test and cfd techniques for retro-propulsion (RETPRO): Overview on a project within the future launchers preparatory programme (flpp). In *Conference: International Conference on Flight Vehicles, Aerothermodynamics and Re-entry Missions & Engineering (FAR)*, Monopoli, Italy, October 2019.

DOI: 10.13009/EUCASS2023-638

[8] Matthew T. Vernacchia and Kelly J. Mathesius. Strategies for reuse of launch vehicle first stages. In *69th International Astronautical Congress 2018*, Bremen, DE, 2018. IAC-18-D2.4.3.

[9] Satoshi Nonaka, Hiroyuki Nishida, Hiroyuki Kato, Hiroyuki Ogawa, and Yoshifumi Inatani. Vertical landing aerodynamics of reusable rocket vehicle. *TRANSACTIONS OF THE JAPAN SOCIETY FOR AERONAUTICAL AND SPACE SCIENCES, AEROSPACE TECHNOLOGY JAPAN*, 10(0):1–4, 2012.

[10] Ashley M. Korzun and Louis A. Cassel. Scaling and similitude in single nozzle supersonic retropropulsion aerodynamics interference. In *AIAA Scitech 2020 Forum*, Orlando, FL, USA, jan 2020. American Institute of Aeronautics and Astronautics.

[11] G. P. Sutton and O. Biblarz. *ROCKET PROPULSION ELEMENTS*, chapter Ch. 3, "Nozzle Theory and Thermodynamic Relations", pages pp. 50,62–63,72. WILEY, Wiley, Hoboken, NJ, USA, ed. 9 edition, October 2016.

[12] Kevin Gutsche, Ansgar Marwege, and Ali Gülhan. Similarity and key parameters of retropropulsion assisted deceleration in hypersonic wind tunnels. *Journal of Spacecraft and Rockets*, 58(4):984–996, jul 2021.

[13] G. S. Settles. Toepler's schlieren technique. In *Schlieren and Shadowgraph Techniques*, pages 39–75. Springer Berlin Heidelberg, 2001.

[14] Martin Leonhardsberger and Peter Strohmer. Internal report: Vacuum wind tunnel facility. Technical report, Technische Universität Dresden, 2004.

[15] Marco Garutti. Numeric comparative study on advanced nozzles in subsonic counter-flows. Master's thesis, Universitá degli Studi di Padova, Technische Universität Dresden, 2023.

[16] C. C. Lee. Technical note - fortran programs for plug nozzle design. Technical report, Scientific Research Laboratories, Brown Engineering Company, Inc., March 1963.

[17] M. Onofri, M. Calabro, G. Hagemann, H. Immich, P. Sacher, F. Nasuti, and P. Reijasse. Plug nozzles: summary of flow features and engine performance - overview of RTO/AVT WG 10 subgroup 1. In *40th AIAA Aerospace Sciences Meeting & Exhibit*, Reno, NV, USA, January 2002. American Institute of Aeronautics and Astronautics.

[18] N. V. Taylor. Simulating cross altitude performance of expansion deflection nozzles. In *57th International Astronautical Congress*, volume 14, 5, pages 620–634, Valencia, SP, October 2006. American Institute of Aeronautics and Astronautics.

[19] Marco Portolani. Investigation of effective altitude compensation of advanced nozzles inretro-flow configurations. Master's thesis, Politecnico di Torino, Technische Universität Dresden, April 2023.

[20] SpaceX. Nrol-85 mission. https://www.youtube.com/watch?v=mMcmf1g4qSA, April 2022.

[21] Ralf Stark. Flow separation in rocket nozzles, a simple criteria. In *41st AIAA/ASME/SAE/ASEE Joint Propulsion Conference & Exhibit*, Tucson, Arizona, USA, July 2005. American Institute of Aeronautics and Astronautics.

[22] Christian Bach, Sarah Schöngarth, Bernhard Bust, Martin Propst, Jan Sieder-Katzmann, and Martin Tajmar. How to steer an aerospike. In *69th International Astronautical Congress (IAC)*, Bremen, Germany, October 2018.

[23] Ansgar Marwege, Christian Hantz, Josef Klevanski, Ali Gülhan, Jan Vos, Dominique Charbonnier, and Sebastian Karl. Retalt1: Aerodynamic data base 2.0, 2022.

[24] Scott A. Berry, Matthew N. Rhode, and Karl Edquist. Supersonic retropropulsion validation experiment in the NASA langley unitary plan wind tunnel. *Journal of Spacecraft and Rockets*, 51(3):664–679, may 2014.

[25] Philip O. Jarvinen and Jacques A. F. Hill. Penetration of retrorocket exhausts into subsonic counterflows. *Journal of Spacecraft and Rockets*, 10(1):85–86, jan 1973.

[26] Ansgar Marwege, Christian Hantz, Daniel Kirchheck, Josef Klevanski, Jan Vos, Mariasole Laureti, Sebastian Karl, and Ali Gulhan. Aerodynamic phenomena of retro propulsion descent and landing configurations. In *2nd International Conference on Flight Vehicles, Aerothermodynamics and Re-entry Missions & Engineering (FAR)*, Zenodo, Heilbronn, Germany, June 2022.

[27] Ansgar Marwege, Daniel Kirchheck, Josef Klevanski, and Ali Gülhan. Hypersonic retro propulsion for reusable launch vehicles tested in the h2k wind tunnel. *CEAS Space Journal*, 14(3):473–499, jun 2022.